$[SrF_{0.8}(OH)_{0.2}]_{2.526}[Mn_6O_{12}]$: Columnar Rock-Salt Fragments Inside the Todorokite-Type Tunnel Structure

Artem M. Abakumov,*,† Joke Hadermann,‡ Gustaaf Van Tendeloo,‡ Maksim L. Kovba,†
Yuri Ya. Skolis,† Svetlana N. Mudretsova,† Evgeny V. Antipov,† Olga S. Volkova,§
Aleksandr N. Vasiliev,§ Natalia Tristan,⊥ Rüdiger Klingeler,⊥ and Bernd Büchner⊥

Department of Chemistry and Low Temperature Physics Department, Moscow State University, 119992 Moscow, Russia, EMAT, University of Antwerp, Groenenborgerlaan 171, B-2020 Antwerp, Belgium, and Leibniz Institute for Solid State and Materials Research (IFW) Dresden, 01171 Dresden, Germany

Received October 20, 2006. Revised Manuscript Received December 30, 2006

A new type of composite structure is described consisting of the todorokite-type $[Mn_6O_{12}]$ framework with large square tunnels accommodating columnar fragments of the rock-salt structure. The crystal structure of the new todorokite-type $[SrF_{0.8}(OH)_{0.2}]_{2.526}[Mn_6O_{12}]$ compound is solved from transmission electron microscopy, and the structure of its anhydrous form $[SrF_{0.8}O_{0.1}]_{2.526}[Mn_6O_{12}]$ is refined from X-ray powder diffraction data. The $[Mn_6O_{12}]$ framework consists of mutually perpendicular walls built of three edge-sharing rutile-type strings of MnO_6 octahedra delimiting large square tunnels with the size of 3 × 3 octahedra. The interior space in the tunnels is filled with rock-salt type $[Sr(F,OH)]_4$ columns. The structure can be interpreted as being an incommensurate composite structure with the modulation vector $\mathbf{q_1} = \gamma\mathbf{c}_1^*$ ($\gamma = 0.63157(3)$) parallel to the direction of tunnel propagation. The octahedral tunnel walls compose subsystem **I** with a $[Mn_6O_{12}]$ composition and a periodicity $c_1 = 2.84$ Å, whereas the $[Sr(F,OH)]_4$ columns belong to subsystem **II** with a periodicity $c_1/\gamma = 4.49$ Å, resulting in a $[Sr(F,OH)]_{4\gamma}[Mn_6O_{12}]$ composition. $[SrF_{0.8}(OH)_{0.2}]_{2.526}[Mn_6O_{12}]$ demonstrates a much larger number of cations inside the tunnels in comparison with the known synthetic and natural marine todorokites. The $[SrF_{0.8}(OH)_{0.2}]_{2.526}[Mn_6O_{12}]$ compound shows a spin-glass behavior below $T^* \approx 26$ K with a dominant antiferromagnetic correlation.

1. Introduction

Natural todorokites $(Na, Ca, K, Ba, Sr)_{0.3-0.7}(Mn, Mg, Al)_6O_{12}\times3.2-4.5H_2O$ belong to the dominant components of ocean Mn nodules and possess some of the largest tunnels among the variety of A_xMnO_2 tunnel manganites (after woodruffite).[1,2] The synthetic analogues of these microporous Mn oxides exhibit a range of potential applications as octahedral molecular sieves, catalysts, matrices for cation intercalation/deintercalation for secondary power sources, and ion-exchange materials for the removal of radionuclides from aqueous radioactive wastes. Until high-resolution electron microscopy and Rietveld refinement were performed, the todorokite structure was a subject of controversy for many years, mainly due to the absence of single crystals and the poor crystallinity of the powder samples.[3−8] The todorokite structure is based on a $[Mn_6O_{12}]$ framework, consisting of rutile-type strings of MnO_6 octahedra. Three edge-sharing strings form a wall; mutually perpendicular walls share corners delimiting square tunnels of the size of 3 × 3 octahedra (Figure 1). The space in the tunnels is occupied by $[M^{+1,+2}(H_2O)_6]$ octahedral strings with water molecules at the corners of the octahedra and the $M^{+1,+2}$ alkali and/or alkali-earth cations at the centers of these octahedra. The water molecules form hydrogen bonds with the oxygen atoms of the tunnel walls.

The tunnel interior in the A_xMnO_2 manganites is filled with cationic species, such as alkali-earth cations, compensating the negative charge of the $[Mn^{+4-\delta}O_2]$ octahedral framework. Square hollandite-type tunnels and the six-sided tunnels of the CaM_2O_4 (M = Ti, Mn, Fe)[9−11] and $CaMn_3O_6$[12] structures incorporate one column of A-cations. The larger "figure-of-eight" and S-shaped tunnels of the $SrMn_3O_6$,[13] $Ba_6Mn_{24}O_{48}$,[14] $CaMn_4O_8$,[15] and $Na_4Mn_9O_{18}$[16,17] structures can

---

* Corresponding author. E-mail: abakumov@icr.chem.msu.ru. Tel: (095) 939-33-75. Fax: (095) 939-47-88.
† Department of Chemistry, Moscow State University.
‡ University of Antwerp.
§ Low Temperature Physics Department, Moscow State University.
⊥ Leibniz Institute for Solid State and Materials Research.

(1) Post, J. E.; Heaney, P. J.; Cahill, C. L.; Finger, L. W. *Am. Mineral.* **2003**, *88*, 1697.
(2) Lei, G. *Mar. Geol.* **1996**, *133*, 103.
(3) Turner, S.; Buseck, P. S. *Science* **1981**, *212*, 1024.
(4) Chukhrov, F. V.; Gorshkov, A. I.; Sivtsov, A. V.; Beresovskaya, V. V. *Nature* **1979**, *278*, 631.
(5) Miura, H. *J. Hokkaido Univ., Fac. Sci., Ser. 4: Geol. Mineral.* **1991**, *23*, 41.
(6) Post, J. E.; Bish, D. L. *Am. Mineral.* **1988**, *73*, 861.
(7) Post, J. E.; Heaney, P. J.; Hanson, J. *Am. Mineral.* **2003**, *88*, 142.
(8) Burns, R. G.; Burns, V. M.; Stockman, H. W. *Am. Mineral.* **1983**, *68*, 972.
(9) Bertaut, F.; Blum, P. *J. Phys.* **1956**, *17*, 517.
(10) Giesber, H. G.; Pennington, W. T.; Kolis, J. W. *Acta Crystallogr., Sect. C* **2001**, *57*, 329.
(11) Decker, D. F.; Kasper, J. S. *Acta Crystallogr.* **1957**, *10*, 332.
(12) Hadermann, J.; Abakumov, A. M.; Gillie, L. J.; Martin, C.; Hervieu, M. *Chem. Mater.* **2006**, *18*, 5530.
(13) Gillie, L. J.; Hadermann, J.; Perez, O.; Martin, C.; Hervieu, M.; Suard, E. *J. Solid State Chem.* **2004**, *177*, 3383.
(14) Boullay, Ph.; Hervieu, M.; Raveau, B. *J. Solid State Chem.* **1997**, *132*, 239.

10.1021/cm062508s CCC: $37.00

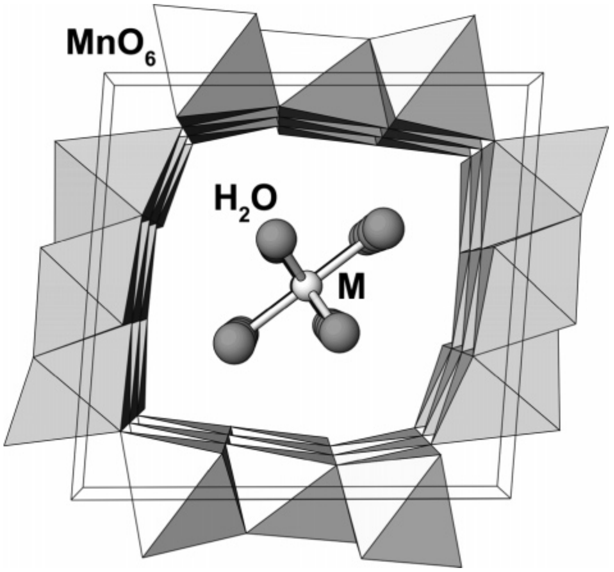

Figure 1. Crystal structure of todorokite $M_xMn_6O_{12}\times yH_2O$.

accommodate from two to four A-cationic columns. These cations are at sufficiently short distance from the tunnel walls to form ionic bonds to the oxygen atoms. However, in the todorokite structure, the oxygen atoms of the walls cannot effectively coordinate the cation column because of the significantly larger distance between opposite walls and to the tunnel center. One can assume that the large todorokite-type tunnels provide enough space to accommodate positively charged columnar fragments of other structures, which can stabilize the $[Mn_6^{+4-\delta}O_{12}]$ framework, playing the same role as the cationic columns in the narrower tunnels. In this contribution, we describe the novel $[SrF_{0.8}(OH)_{0.2}]_{2.526}$-$[Mn_6O_{12}]$ tunnel manganite with a composite structure comprising a $[Mn_6O_{12}]$ todorokite-type framework filled with [SrX] ($X = F^-$, OH^-) columnar fragments of the rock-salt structure. This new structural organization of the tunnel interior leads to a much larger number of cations inside the tunnels compared to that in the known synthetic and natural todorokites.

2. Experimental Section

2.1. Synthesis. $SrCO_3$, SrF_2, MnO_2, Mn_2O_3 (“very pure” purity grade, Reakhim), and preliminary synthesized $SrMn_3O_6$ were used as initial reagents. Prior to annealing, the initial mixtures of the reagents were ground in an agate mortar, pressed into pellets, placed in alumina crucibles, and degassed in a silica tubular reactor at 300 °C and $P = 1 \times 10^{-3}$ mbar in order to remove traces of water. The targeted compound was prepared using two different routes:

(1) the $1.5SrCO_3 + SrF_2 + 3Mn_2O_3$ initial mixture was annealed in a dried oxygen flow at 900 °C for 60−70 h several times with intermediate regrindings until an overall time of 250−300 h was reached;

(2) the $1.5SrMn_3O_6 + SrF_2 + 1.5MnO_2$ initial mixture was sealed into an O_2-filled silica tube with an extra amount of MnO_2 in a separate crucible in order to create the required oxygen pressure and annealed at 800 °C for 200 h with intermediate regrindings.

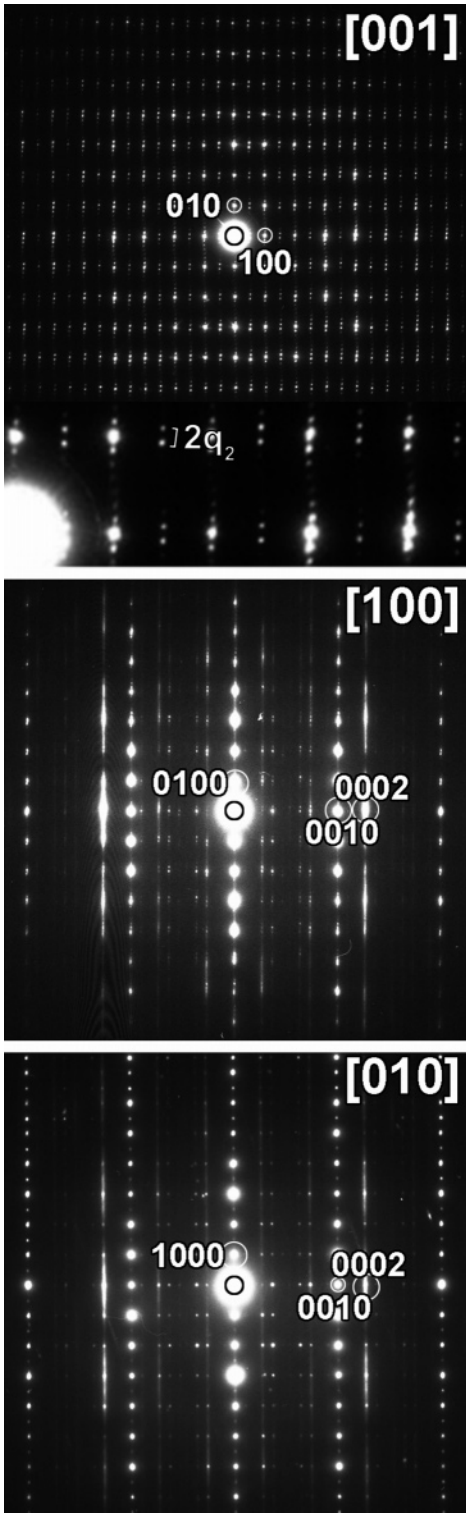

Figure 2. Electron diffraction patterns of $[SrF_{0.8}(OH)_{0.2}]_{2.526}[Mn_6O_{12}]$. The indexing is performed with four *hklm* indices and the $\mathbf{q}_1$ modulation vector. The enlarged part on the [001] ED pattern shows the satellite positions corresponding to the $\mathbf{q}_2$ modulation vector.

Independently from the synthesis routine used, all obtained samples exhibit the same XRD patterns.

2.2. Chemical Analysis. The formal Mn valence was determined by iodometric titration. The fluorine content was determined by the electromotive force (EMF) method with solid F^- electrolyte at 1173 K. Thermogravimetric (TG) and differential scanning calo-

---

(15) Barrier, N.; Michel, C.; Maignan, A.; Hervieu, M.; Raveau, B. *J. Mater. Chem.* **2005**, *15*, 386.

(16) Parant, J.-P.; Olazcuaga, R.; Devalette, M.; Fouassier, C.; Hagenmuller, P. *J. Solid State Chem.* **1971**, *3*, 1.

(17) Floros, N.; Michel, C.; Hervieu, M.; Raveau, B. *J. Solid State Chem.* **2001**, *162*, 34.

rimetric (DSC) measurements were performed in a dried oxygen flow on a NETZSCH STA 409 thermoanalyzer in the temperature range from 20 to 1000 °C with a heating/cooling rate of 10 °C/min.

2.3. X-ray Powder Diffraction. X-ray powder diffraction (XRD) data were collected on a Huber G670 Guinier diffractometer and a STADI-P diffractometer ($CuK_{\alpha 1}$-radiation, curved Ge monochromator, transmission mode). High-temperature XRD patterns were obtained with a SIEMENS D500 powder diffractometer (CuK_{α} radiation, graphite monochromator, reflection mode). The JANA2000 program package was used for the Rietveld structure refinement.[18]

2.4. Transmission Electron Microscopy. Electron diffraction (ED) studies were performed using a Phillips CM20 microscope and high-resolution electron microscopy (HREM) using a JEOL 4000EX. Energy-dispersive X-ray (EDX) spectra were obtained on the Phillips CM20 with an Oxford INCA system. The HREM images were simulated by means of the MacTempas software.

2.5. Specific Heat, Magnetic Susceptibility, and Magnetization Measurements. The measurements were performed in a range of 2−350 K. The temperature dependence of the specific heat was measured by Physical Properties Measurement System, Quantum Design. The temperature dependence of the magnetic susceptibility was taken in zero-field cooling (ZFC) and field-cooling (FC) regimes by a SQUID magnetometer (Magnetic Properties Measurement System, Quantum Design). The field dependence of the magnetization was measured by a vibrating sample magnetometer, EG&G PARC.

3. Results

3.1. Electron and X-ray Diffraction: The Lattice Parameters. From the ED study it becomes clear that the obtained compound has an incommensurate composite structure. The composition and structural organization of this compound will be further discussed in detail, and for now, the $[SrF_{0.8}(OH)_{0.2}]_{2.526}[Mn_6O_{12}]$ notation will be used to identify it. A set of strong sharp diffraction spots can be selected on the [001], [100], and [010] ED patterns of $[SrF_{0.8}(OH)_{0.2}]_{2.526}[Mn_6O_{12}]$ (Figure 2); the positions of these spots match with the primitive tetragonal lattice with $a \approx 9.8$ Å, $c_1 \approx 2.8$ Å. These reflections belong to subsystem **I** of the composite structure. A second set of diffraction spots and diffuse intensity lines parallel to the $\mathbf{a}^*$ and $\mathbf{b}^*$ axes are present, passing through these spots. They are the main reflections from subsystem **II** with $a \approx 9.8$ Å, $c_2 \approx 4.5$ Å and the satellites arising from mutual modulations of both subsystems. The indexation of both reflection sets was performed with the diffraction vector $\mathbf{H} = h\mathbf{a}^* + k\mathbf{b}^* + l\mathbf{c}_1^* + m\mathbf{q}_1$, where $\mathbf{q}_1 = \mathbf{c}_2^* = \gamma\mathbf{c}_1^*$, $\gamma \approx 0.632$. The relation between the subsystems is established by the interlattice matrix[19]

$$W^2 = \begin{pmatrix} 1 & 0 & 0 & 0 \\ 0 & 1 & 0 & 0 \\ 0 & 0 & 0 & 1 \\ 0 & 0 & 1 & 0 \end{pmatrix}$$

Thus both subsystems have a common mesh in the (001)* reciprocal lattice plane and different lengths of the reciprocal lattice vectors $\mathbf{c}_1^*$ and $\mathbf{c}_2^*$. Being indexed with four *hklm* indexes, the reflections can be separated into four sets: the *hkl*0 reflections belong to subsystem **I**, the *hk*0*m* reflections belong to subsystem **II**, the *hk*00 reflections form a common part of both subsystems, and the *hklm* reflection are the satellites (parts a and b of Figure 3).

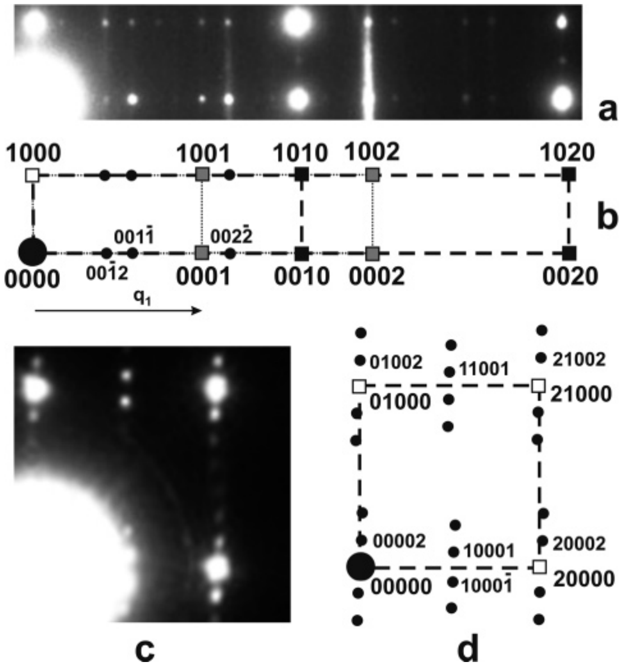

Figure 3. (a) Enlarged part of the [010] ED pattern. (b) Indexation scheme of the [010] ED pattern with four *hklm* indices. (c) Enlarged part of the [001] ED pattern. (d) Indexation scheme of the [001] ED pattern with five *hklmn* indices and $\mathbf{a}'^* = 1/2\mathbf{a}^*$. Open squares mark the reflections common for the subsystems **I** and **II**. Black and gray squares stand for the main reflections of the subsystems **I** and **II**, respectively. Small black circles are the satellites.

The diffuse streaks associated with subsystem **II** were observed in all [*hk*0] zones, which is characteristic for diffuse intensity planes perpendicular to $\mathbf{c}^*$. Such diffuse intensity distribution suggests that atomic columns of subsystem **II** are characterized by long-range order along the *c*-axis with only small correlations along the perpendicular directions. The absence of diffuse intensity for the reflections from subsystem **I** indicates a well-established order for that subsystem. The degree of disorder in subsystem **II** is different for different crystallites, and many ED patterns were observed in which the diffraction from subsystem **II** shows no sharp reflections but only lines of diffuse intensity.

The [001] ED pattern also shows a dense set of satellite reflections, which form linear arrays associated with each basic spot and with the intermediate ($^1/_2 n\mathbf{a}^* + m\mathbf{b}^*$) positions. These satellites cannot be indexed with the modulation vector $\mathbf{q}_1$ and require a doubling of the *a* parameter and an extra modulation vector $\mathbf{q}_2 = \alpha\mathbf{a}'^* + \beta\mathbf{b}^*$ ($\mathbf{a}'^* = {}^1/_2\mathbf{a}^*$). A modulation vector with two irrational α and β components is incompatible with the tetragonal symmetry and decreases it down to monoclinic. The complete indexing of the ED patterns has to be performed with five *hklmn* indices according to $\mathbf{H} = h\mathbf{a}'^* + k\mathbf{b}^* + l\mathbf{c}_1^* + m\mathbf{q}_1 + n\mathbf{q}_2$, $a' \approx 19.6$ Å, $b \approx 9.8$ Å, $c_1 \approx 2.8$ Å, $\mathbf{q}_1 \approx 0.632\mathbf{c}_1^*$, $\mathbf{q}_2 \approx 0.018\mathbf{a}'^* + 0.08\mathbf{b}^*$. The indexation scheme of the [001] ED pattern is shown in parts c and d of Figure 3. The reflection

---

(18) Petricek, V.; Dusek, M. *JANA2000: Programs for Modulated and Composite Crystals*; Institute of Physics: Praha, Czech Republic, 2000.

(19) Van Smaalen, S. *Phys. Rev. B* **1981**, *43*, 11330.

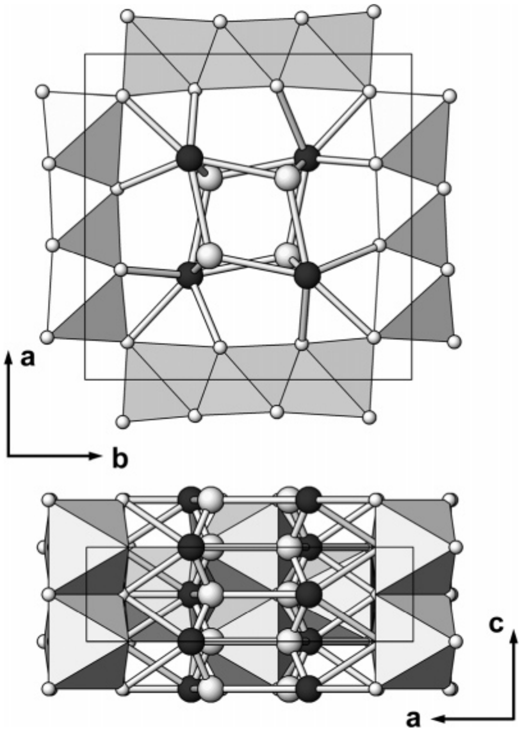

Figure 4. Basic $[SrF_{0.8}(OH)_{0.2}]_{2.526}[Mn_6O_{12}]$ structure. The Mn atoms are located at the octahedra; the Sr atoms and anions in the tunnels are shown as black and gray spheres, respectively. On the [010] projection, the front octahedral wall is omitted for clarity.

condition *hklmn*: $h + n = 2n$ is satisfied, suggesting the centering vector $^1/_2$,0,0,0,$^1/_2$.

The small value of the α component of the modulation vector causes the satellite arrays to be aligned almost parallel to the **b*** axis, and their relrods result in weak spots at the $\mathbf{H} \pm {}^1/_2\mathbf{a}^*$ positions in the [010] zone. The intensity of these spots increases with the distance from the central spot because the satellites approach the exact Bragg position due to the curvature of the Ewald sphere.

The geometry of the [001] diffraction pattern is typical for a periodic arrangement of translation interfaces with the displacement vector $\mathbf{R} = [^1/_2, 0, w]$. The interfaces are oriented nearly parallel to the *b*-axis and exhibit a periodical "ledging". The average interplanar spacing for these antiphase boundaries is $d \approx 89$ Å.

The reciprocal lattice revealed from the ED patterns was used to interpret the XRD pattern. It was possible to index all strong reflections assuming a composite structure with a tetragonal unit cell with $a = 9.7842(5)$ Å, $c_1 = 2.8403(2)$ Å, $\mathbf{q}_1 = 0.63157(3)\mathbf{c}_1^*$ (refined using the LeBail method). Introducing the second modulation vector $\mathbf{q}_2$ and doubling the *a*-parameter allows for the complete indexation of the XRD pattern. The LeBail refinement results in the lattice parameters $a = 19.6054(4)$ Å, $b = 9.7767(2)$ Å, $c_1 = 2.84243(5)$ Å, $\gamma = 90.225(2)^o$, $\mathbf{q}_1 = 0.63186(2)\mathbf{c}_1^*$, $\mathbf{q}_2 = 0.0176(1)\mathbf{a}^* + 0.07497(5)\mathbf{b}^*$, in excellent agreement with the ED data.

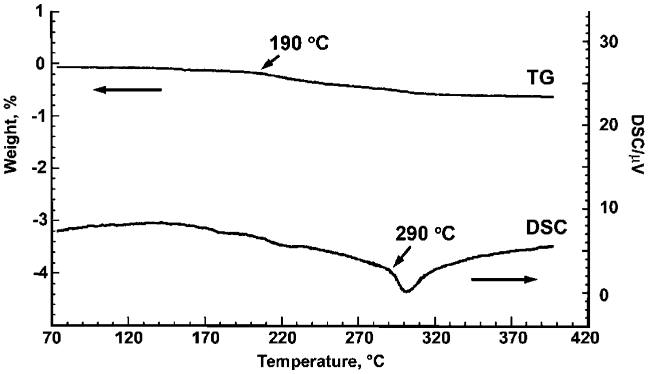

Figure 5. TG and DSC curves for $[SrF_{0.8}(OH)_{0.2}]_{2.526}[Mn_6O_{12}]$ measured on heating in oxygen flow.

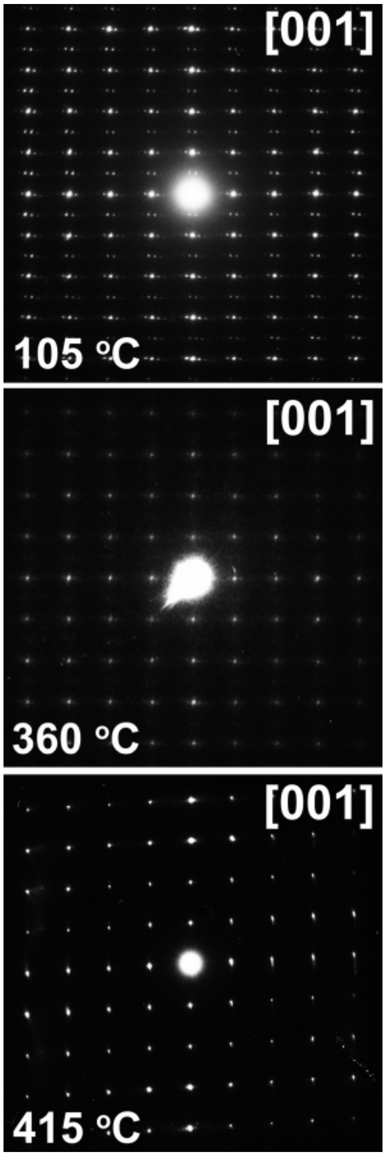

Figure 6. [001] ED pattern recorded at different temperatures. The upper and lower patterns correspond to the LT and HT phases, respectively.

3.2. Structure Model and Chemical Composition. The primary structure model for $[SrF_{0.8}(OH)_{0.2}]_{2.526}[Mn_6O_{12}]$ was deduced from HREM observations. Such [001] HREM images are shown in Figure 10 (top). Temporarily assuming that the dark areas on the image correspond to a high scattering density, it is easy to identify a pattern of 3 × 3 square tunnels. Four extra atomic columns are located inside the tunnels. This pattern of tunnels shows a close resemblance to the atomic arrangement in the todorokite structure (Figure 1).[6,7] However, in contrast to todorokites, four cation columns are visible on the [001] HREM image of $[SrF_{0.8}$-

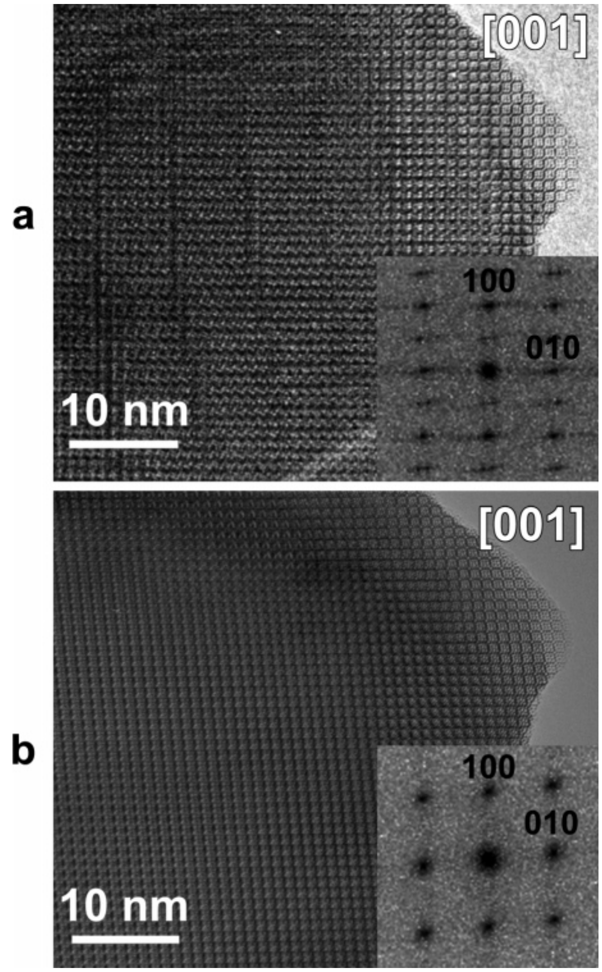

Figure 7. [001] overview HREM images of the (a) LT and (b) HT phases along with the Fourier transforms (shown as insets).

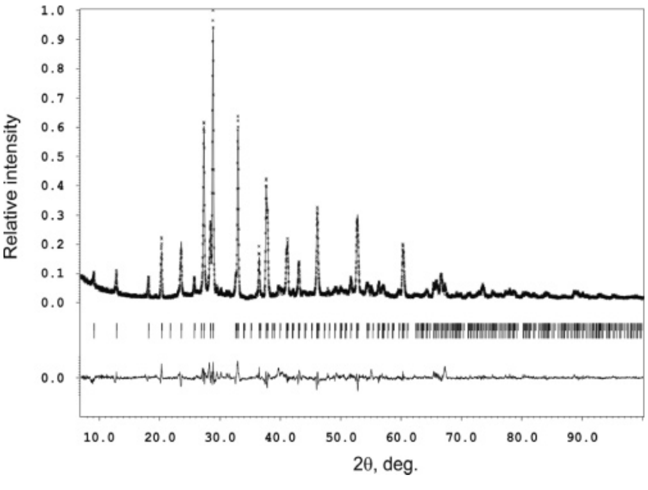

Figure 8. Experimental, calculated, and difference X-ray diffraction profiles for $[SrF_{0.8}O_{0.1}]_{2.526}[Mn_6O_{12}]$.

$(OH)_{0.2}]_{2.526}[Mn_6O_{12}]$ at the positions (x,x,z), $(-x,x,z)$, $(x,-x,z)$ and $(-x,-x,z)$ with $x \approx 0.33$ (if the origin is placed at the cross point of the walls). In todorokites, these positions correspond nearly to those of the water molecules and the single-cation column is located at the $(^1/_2,^1/_2,z)$ position. This means that in the $[SrF_{0.8}(OH)_{0.2}]_{2.526}[Mn_6O_{12}]$ structure, the position of the water molecules is occupied by the Sr cations. In such a structure, the coordination environment of the Sr atoms is incomplete and asymmetric because only the anions of two neighboring walls form bonds to them. Extra anions X completing the Sr coordination environment can be placed between two Sr atoms along the tunnel direction, so that a −Sr−X−Sr−X−Sr− column is formed running along the *c*-axis. Such atomic arrangement built in the space group $P4_2/m$ is shown in Figure 4.

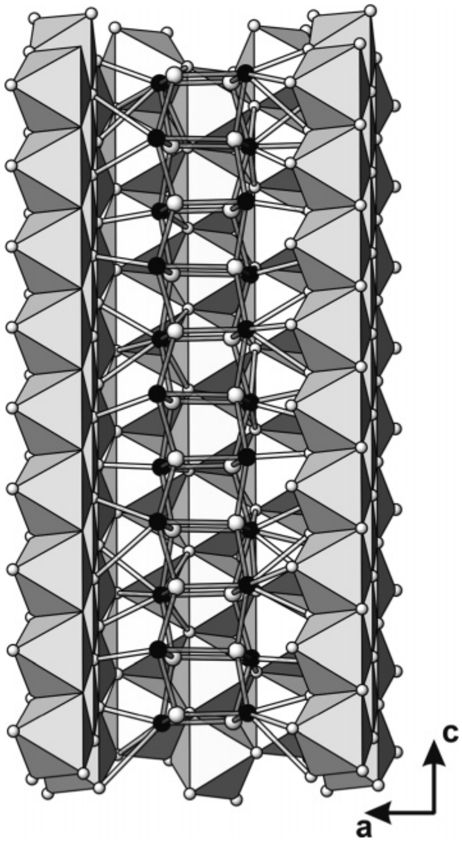

Figure 9. Composite $[SrF_{0.8}O_{0.1}]_{2.526}[Mn_6O_{12}]$ structure. The octahedral walls represent the $[Mn_6O_{12}]$ subsystem. The $[Sr(F,O)]_4$ subsystem with rock-salt structure is imaged as spheres with bonds. The Mn atoms are located at the octahedra; the Sr atoms and anions in the tunnels are shown as black and gray spheres, respectively. The front octahedral wall is omitted for clarity.

The Sr−X distances are unreliably short in this structure and the Sr−X columns must be expanded along the *c*-axis. The octahedral $[Mn_6O_{12}]$ framework can be considered as subsystem **I** in the composite structure, whereas the four [SrX] strings belong to subsystem **II**. The modulation vector $\mathbf{q}_1$ then determines the expansion degree of subsystem **II** with respect to subsystem **I**. The average repeat period of subsystem **II** is $c_2 = c_1/\gamma = 4.49$ Å, which results in significantly increased Sr−Sr and Sr−X separations. Taking into account that the cell volume ratio for the subsystems **I** and **II** V_I/V_{II} is equal to $\gamma = 0.63157(3)$ (as refined with the Le Bail method from the XRD data for a tetragonal unit cell), the expected phase composition is therefore $[SrX]_{4\gamma}[Mn_6O_{12}]$ or $[SrX]_{2.5263(1)}[Mn_6O_{12}]$ (this will be further denoted as $[SrX]_{2.526}[Mn_6O_{12}]$).

This composition was confirmed by different analytical techniques. The Sr:Mn ratio of 0.41(2) was measured using EDX analysis, and this is very close to the bulk composition of the samples and the Sr:Mn = 0.421 ratio calculated from the γ value. Measurements of the EMF values of three solid electrochemical cells, containing equilibrated mixtures of the

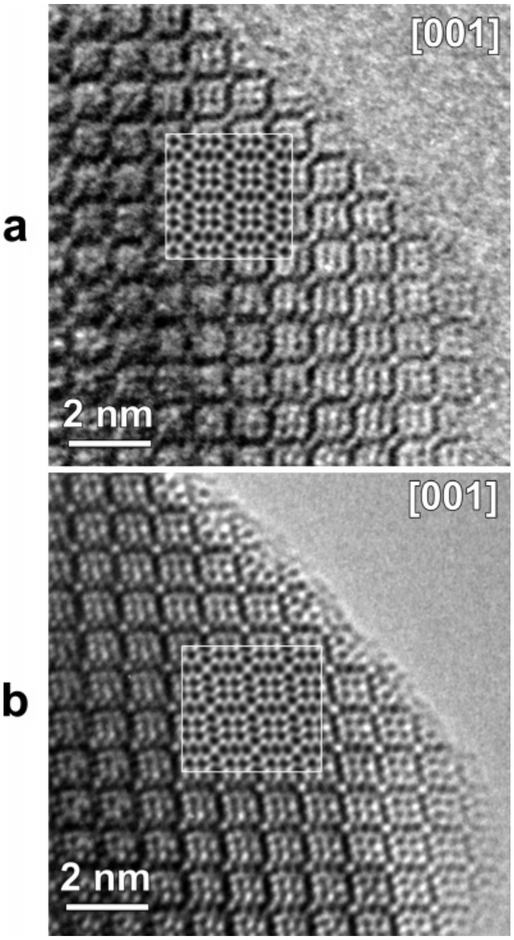

Figure 10. [001] HREM images of the (a) LT and (b) HT phases. The calculated images ($\Delta f = -300$ Å, $t = 20$ Å) are shown as insets.

$[SrX]_{2.526}[Mn_6O_{12}]$ phase with its equilibrium neighbors $SrMn_3O_6$, Mn_2O_3 and SrF_2 (see the Supporting Information for details) resulted in a fluorine content of 2.02(6) F atoms per $[SrX]_{2.526}[Mn_6O_{12}]$ formula. The oxidation state of the Mn atoms $V_{Mn} = +3.6$ was determined using iodometric titration. TGA measurements in a dried O_2 flow revealed nearly 0.5% irreversible weight loss in the temperature range of 190−350 °C, which can be attributed to the loss of H_2O. This weight loss corresponds to 0.22 water molecules per formula unit, and it is reasonable to assume that they fill the X positions together with fluorine in the form of hydroxyl groups OH^-. Therefore, the final chemical composition is assigned as $[SrF_{0.8}(OH)_{0.2}]_{2.526}[Mn_6O_{12}]$.

The shape of the diffuse intensity associated with the subsystem **II** indicates that the atomic arrangement in the $[SrF_{0.8}(OH)_{0.2}]_4$ columns is well-ordered along the *c*-axis, but only small correlations are present between the columns on going from tunnel to tunnel. The *z* positions of some $[SrF_{0.8}(OH)_{0.2}]_4$ columns are different from the z positions of other $[SrF_{0.8}(OH)_{0.2}]_4$ columns because of weak interaction between the columns in the adjacent tunnels. Such a kind of disorder is typical for the A_xBO_2 tunnel structures with the hollandite-type tunnels.[14,20,21]

3.3. Phase Transformations. $[SrF_{0.8}(OH)_{0.2}]_{2.526}[Mn_6O_{12}]$ exhibits a sequence of phase transformations upon heating. The TG-DSC curves were measured in the temperature range 70−1000 °C in oxygen flow (Figure 5). The compound starts to lose weight at ~190 °C, and the weight loss increases continuously up to ~ 350 °C. At 290 °C, there is a pronounced peak in the DSC curve, indicating a phase transition. These effects are absent on the TG-DSC curves measured on cooling and subsequent heating. Above 400 °C, no effects were observed until the decomposition temperature of 930 °C was reached. The fact that the observed phase transition is irreversible and associated with water removal allows us to relate it to the structural changes caused by the presence of hydroxyl groups in the tunnels.

The structural changes were investigated by monitoring the ED patterns while heating the sample in situ in the electron microscope. The satellites, clearly seen on the [001] ED pattern at room temperature and at 105 °C, disappear at 360 °C, leaving only a weak diffuse intensity (Figure 6). This indicates a suppression of the long-range order related to the periodic arrangement of the antiphase boundaries. However, in contrast to the TG-DSC measurements, a further transformation is observed if the sample is held at 350−450 °C for longer time. The [001] ED pattern taken at 415 °C shows a complete absence of the satellite reflections corresponding to the $\mathbf{q}_2$ modulation vector and a pronounced monoclinic distortion (Figure 6). The initial room temperature [001] ED pattern is not restored upon cooling, which shows that these transformations are irreversible. High-temperature ED observations of the [100] and [010] zones reveal that the $\mathbf{q}_1$ vector is not altered at these transitions. The lattice parameters of the high-temperature phase measured from the ED patterns after cooling to room temperature are $a \approx 9.72$ Å, $b \approx 9.55$ Å, $c_1 \approx 2.84$ Å, $c_2 \approx 4.49$ Å, $\gamma \approx 95.6^o$.

A high-temperature X-ray diffraction experiment performed in air at 400 °C did not confirm the drastic increase in the monoclinic distortion. Weak satellites corresponding to the $\mathbf{q}_2$ modulation vector vanish at this temperature, but no detectable reflection splitting appears. The discrepancy between the TG-DSC, high-temperature XRD, and high-temperature ED observations can be explained by the significantly different environmental conditions inside the electron microscope, where the sample is heated in a dynamic vacuum of $\sim 1 \times 10^{-7}$ mbar. This causes both the elimination of water and oxygen loss that leads to a progressive monoclinic distortion, not detected when the measurements were done at higher partial oxygen pressures.

It is found that the energy of the electron beam required for HREM imaging is sufficient to induce the transition from the low temperature (LT) phase to the high-temperature (HT) monoclinic phase. The [001] HREM images of the LT phase (Figure 7a) are taken, keeping sample irradiation at a minimum. At low magnification, the antiphase boundaries are clearly visible and the satellite reflections show up on the corresponding Fourier transform. When the electron beam is focused, the [001] HREM image of the HT phase is recorded (Figure 7b). The tunnel structure and the arrangement of the columns in the tunnels are preserved at the phase transformation. The antiphase boundaries have disappeared

---

(20) Wu, X.-J.; Fujiki, Y.; Ishigame, M.; Horiuchi, S. *Acta Crystallogr., Sect. A* **1991**, *47*, 405.

(21) Carter, M. L.; Withers, R. L. *J. Solid State Chem.* **2005**, *178*, 1903.

Table 1. Selected Parameters from Rietveld Refinement of the [SrF$_{0.8}$O$_{0.1}$]$_{2.526}$[Mn$_6$O$_{12}$] Structure

(3 + 1)D space group	$P4_2/m(00\gamma)s0$
a (Å)	9.8181(2)
c (Å)	2.8565(1)
q	0.63151(7)**c***
cell volume (Å^3)	275.36(1)
Z	1
calcd density (g/cm^3)	4.745
T (°C)	400
2θ range, step (deg)	$7 \leq 2\theta \leq 100$, 0.02
radiation, λ (Å)	CuK$_\alpha$, 1.5418
no. of main reflns	339
no. of refinable params	18
R_I, R_P, R_{wP}	0.056, 0.097, 0.135

Table 2. Atomic Coordinates and Atomic Displacement Parameters for [SrF$_{0.8}$O$_{0.1}$]$_{2.526}$[Mn$_6$O$_{12}$]

atom	x	y	z	U_{iso} (Å^2)
		Subsystem **I**, [Mn$_6$O$_{12}$]		
Mn1	0	0.5	0	0.018(3)
Mn2	0.7699(4)	0.0094(7)	0	0.018(3)
O1	0.918(1)	0.161(2)	0	0.019(3)
O2	0.422(1)	0.103(1)	0	0.019(3)
O3	0.898(2)	0.667(1)	0	0.019(3)
		Subsystem **II**, [SrF$_{0.8}$O$_{0.1}$]$_4$		
Sr1	0.660(1)	0.3368(9)	0	[b]
F1[a]	0.376(2)	0.406(3)	0	0.011(9)
u_{11}	u_{22}	u_{33}	u_{12}	u_{13}
0.109(9)	0.001(5)	0.296(9)	−0.007(3)	0

[a] F1 = F$_{0.8}$O$_{0.1}$. [b] Anisotropic atomic displacement parameters for the Sr1 atom.

Table 3. Selected Interatomic Distances (Å) for [SrF$_{0.8}$O$_{0.1}$]$_{2.526}$[Mn$_6$O$_{12}$]

Mn1−O2	1.907(9) × 4	Sr1−O1$_{min}$	3.07(2)
Mn1−O3	1.92(2) × 2	Sr1−O2$_{min}$	2.86(2) × 2
Mn2−O1	2.08(1) × 1	Sr1−O2$_{min}$	2.48(2)
Mn2−O1	1.82(2) × 2	Sr1−O3$_{min}$	2.71(2) × 2
Mn2−O2	2.18(2) × 1	Sr1−O3$_{min}$	2.30(2)
Mn2−O3	1.97(1) × 2	Sr1−F1	2.87(3) × 1
		Sr1−F11	2.54(3) × 1
		Sr1−F1	2.385(9) × 2

in the HT phase and no satellites are present in the corresponding Fourier transform.

3.4. Rietveld Refinement. A Rietveld refinement of the [SrF$_{0.8}$(OH)$_{0.2}$]$_{2.526}$[Mn$_6$O$_{12}$] structure from X-ray powder diffraction data taking into account the monoclinic symmetry, the doubling of the a-parameter and both modulations with the $\mathbf{q}_1$ and $\mathbf{q}_2$ vectors cannot be reliably performed because of the extremely dense set of reflections resulting in a high degree of overlap. To eliminate the diffraction effects related to the modulations in the ab plane, we took the XRD pattern for the refinement at 400 °C, i.e., above the phase transition point. The initial model for the refinement was constructed using the (3 + 1)D space group $P4_2/m(00\gamma)s0$ (a nonstandard setting of the (3 + 1)D space group $P4_2/m(00\gamma')00$ related by $\gamma' = \gamma - 1$), which is the symmetry group of both subsystems. The scattering factor for the anion position of subsystem **II** was set as being equal to that of fluorine because the fluorine and oxygen atoms have very close scattering power. Since the XRD pattern for the refinement was taken after water elimination from the sample, the occupancy factor of the anion position was assumed to be 0.9 according to the chemical composition [SrF$_{0.8}$O$_{0.1}$]$_{2.526}$[Mn$_6$O$_{12}$] of the anhydrous sample. Displacive modulations can be expected along the c-axis, but the refinement of the coefficients of the displacive modulation functions in either a harmonic approximation or as sawtooth functions did not result in physically sensible values because of the disorder in subsystem **II**. The final refinement was done with an isotropic approximation for the atomic displacement parameters (ADPs) for all atoms except Sr1. The ADP of the Sr1 atom is highly anisotropic, with a large u_{33} component that is related to the strong disorder in subsystem **II**. The crystallographic and atomic parameters and the most relevant interatomic distances are given in Tables 1−3 . Figure 8 represents the experimental, calculated, and difference XRD profiles.

The Rietveld refinement confirms the proposed todorokite-based structure (Figure 9). The Mn1O$_6$ octahedron is characterized by six almost-equivalent Mn1−O distances, whereas the Mn2O$_6$ octahedron is distorted with Mn2−O distances between 1.82 and 2.18 Å. As for the composite structure, there is no upper limit on the Sr1−O distances, because these atoms belong to different subsystems, and only minimal Sr1−O separations are listed in Table 3. The amount of oxygen neighbors for the Sr1 atoms varies from 2 with short Sr1−O distances (d(Sr1−O2) = 2.48 Å × 1, d(Sr1−O2) = 2.30 Å × 1) to 5 with longer distances (d(Sr1−O1) = 3.07 Å × 1, d(Sr1−O3) = 2.64 Å × , d(Sr1−O2) = 2.85 Å × 2). The coordination environment of the Sr1 atoms is completed by four F1 atoms; two of them are positioned above and below the Sr1 atom along the [SrF1] (F1 = F, O) chain and another two belong to the two neighboring chains. In fact, the atomic arrangement of subsystem **II** represents part of a distorted rock-salt type structure. The bond valence sum for the Sr1 atoms varies from +1.80 to +2.14 with an average value of +1.95.

For the simulation of the HREM images, the atomic positions were transformed to a 3D unit cell with a 12 times larger c-parameter and $P1$ symmetry. In order to get the atomic coordinates for the HT phase, a monoclinic distortion with $\gamma = 95.6^{o}$ was introduced. In both cases, the calculated [001] HREM images at the focus value $\Delta f = -300$ Å and thickness $t = 20$ Å are in excellent agreement with the experimental ones (Figure 10). On these images, the dark dots correspond to the projections of the Mn and Sr columns. The [100] HREM image of [SrF$_{0.8}$(OH)$_{0.2}$]$_{2.526}$[Mn$_6$O$_{12}$] is shown in Figure 11 along with the calculated image ($\Delta f = -590$ Å, $t = 80$ Å). Under these imaging conditions, the bright dots originate from low scattering areas on the structure projection. The darker stripes correspond to the projection of the tunnel walls, parallel to the viewing direction. The modulation is seen as a variation of the brightness of the dots, which has an irregular character, in agreement with the disorder in subsystem **II**.

3.5. Thermodynamical and Magnetic Properties. The temperature dependence of the specific heat C of [SrF$_{0.8}$(OH)$_{0.2}$]$_{2.526}$[Mn$_6$O$_{12}$], shown in Figure 12a, demonstrates an anomaly at $T^* \approx 26$ K, tentatively ascribed to the formation of a spin-glass-like state. The C/T vs T^2 dependence, shown in the inset of Figure 12a, does not allow us to estimate the electronic contribution, because this quantity approaches zero at low temperature, indicating the freezing out of free carriers. Because the magnon and phonon contributions to the specific

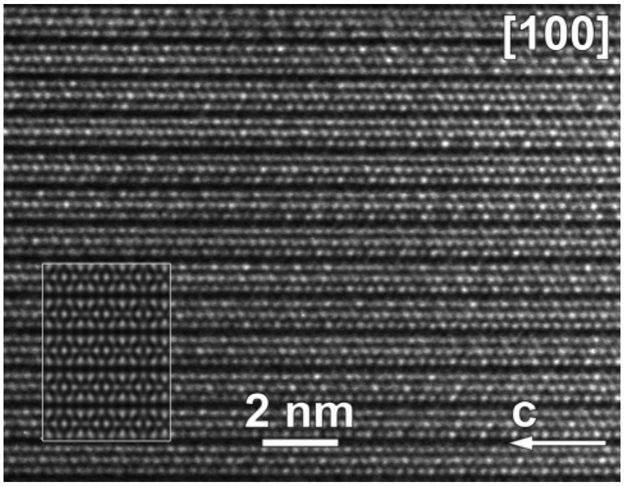

Figure 11. [100] HREM image of $[SrF_{0.8}(OH)_{0.2}]_{2.526}[Mn_6O_{12}]$. The calculated image ($\Delta f = -590$ Å, $t = 80$ Å) is shown as an inset.

heat in a magnetically ordered state are additive to each other, the reliable estimation of the Debye temperature cannot be made from the existing data. However, the high-temperature data on the specific heat imply a Θ_D significantly higher than room temperature.

The temperature dependences of the magnetic susceptibility χ of $[SrF_{0.8}(OH)_{0.2}]_{2.526}[Mn_6O_{12}]$ taken in ZFC and FC regimes are shown in Figure 12b. These curves demonstrate a broad maximum around 30 K and a split below $T^* \approx 26$ K. Such behavior is expected for a transition into a spin-glass-like state. This occurs because of a competition of various exchange interactions between the magnetically active manganese cations.

The temperature dependence of the inverse magnetic susceptibility $1/\chi$ is shown in the lower inset of Figure 12b. At elevated temperatures, the $1/\chi$ vs T dependence obeys the Curie−Weiss law. The effective magnetic moment μ_{eff}, estimated from the slope of $1/\chi$ vs T curve, amounts to 10.9 μ_B. This value is in a good agreement with a theoretical estimation for the effective magnetic moment of 10.6 μ_B in $[SrF_{0.8}(OH)_{0.2}]_{2.526}[Mn_6O_{12}]$ assuming a g-factor equal to 2. The Weiss temperature Θ is found to be −200 K. The large negative value of the Weiss temperature as compared to the temperature of the spin-glass-like state formation T^* indicates the predominance of the antiferromagnetic contribution and the frustration of the exchange interactions. This is supported by the magnetization curve of $[SrF_{0.8}(OH)_{0.2}]_{2.526}[Mn_6O_{12}]$, shown in the upper inset to Figure 12b, which is linear at 5 K up to 15 T.

4. Discussion

The $[SrF_{0.8}(OH)_{0.2}]_{2.526}[Mn_6O_{12}]$ crystal structure can be compared with the structures of other members of the todorokite family. If metal cations enter into the 3 × 3 tunnels of todorokites, they are located at the center of the tunnel surrounded by four columns of H_2O or OH^- groups, which form an octahedral environment for the metal cations. Instead of (H_2O, OH^-) columns, in $[SrF_{0.8}(OH)_{0.2}]_{2.526}[Mn_6O_{12}]$, there are four mixed [Sr, (F, OH^-)] columns, which form a columnar fragment of the rock-salt structure, leaving the position at the center of the tunnels empty. The Sr/Mn = 0.421 ratio in the $[SrF_{0.8}(OH)_{0.2}]_{2.526}[Mn_6O_{12}]$ structure is much higher than the usual ratio in todorokites, where it varies in the range of 0.05−0.12.[6] It shows that potentially the 3 × 3 todorokite-type tunnels can uptake a much larger number of extra cations than generally considered for the natural and synthetic todorokites. The A/B ratio (A is a cation in the tunnels, B is the cation of the tunnel walls) in the composite tunnel structure as found for $[SrF_{0.8}(OH)_{0.2}]_{2.526}[Mn_6O_{12}]$ can be directly inferred from the γ-component of the modulation vector, which determines the volume ratio between the [AX] and $[B_6O_{12}]$ subsystems and the composition as $[SrX]_{4\gamma}[Mn_6O_{12}]$ and hence the A/B ratio as $2/3\gamma$. This also holds for the recently discovered tunnel todorokite-type $Bi_6Rh_{12}O_{29}$ oxide, which can be represented as $[BiO_{0.833}]_3[Rh_6O_{12}]$.[22] This oxide corresponds to the commensurate case of the composite structure with $\gamma = 0.75$ and Bi/Rh = 0.5. In both cases, the expansion of subsystem **II** along the c-axis in comparison with subsystem **I** is required to achieve the appropriate metal−anion distances along the [Sr, (F,OH)] or $[BiO_{0.833}]$ columns.

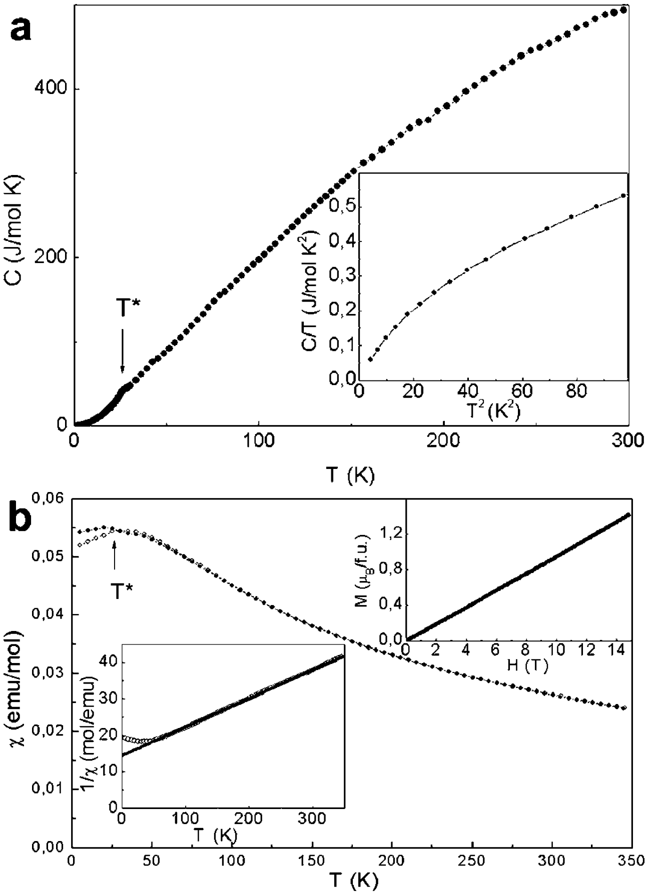

Figure 12. (a) Temperature dependence of specific heat C of $[SrF_{0.8}(OH)_{0.2}]_{2.526}[Mn_6O_{12}]$. Insert, the C/T vs T^2 dependence. (b) Temperature dependences of magnetic susceptibility χ of $[SrF_{0.8}(OH)_{0.2}]_{2.526}[Mn_6O_{12}]$ measured in ZFC (white circles) and FC (black circles) regimes at 0.1 T. Upper insert, the temperature dependence of magnetization M; lower insert, the temperature dependence of the inverse magnetic susceptibility $1/\chi$.

The presence of the OH^- groups is not a necessary condition for the stability of the todorokite-type structure. Indeed, the $[SrF_{0.8}(OH)_{0.2}]_{2.526}[Mn_6O_{12}]$ compound was prepared under conditions that exclude the presence of water,

---

(22) Stowasser, F.; Renkenberger, C. *Z. Kristallogr.* **2006**, *221*, 206.

and it is logical to assume that the water uptake occurs when the as-prepared compound is exposed to air. Water loss at a rather low temperature of 190−350 °C does not destroy the tunnel structure. One can speculate that the satellites with the $\mathbf{q}_2$ modulation vector in the $[SrF_{0.8}(OH)_{0.2}]_{2.526}[Mn_6O_{12}]$ phase arise from the partially ordered distribution of F^- and OH^-. When the structure loses water, this long-range order is destroyed, but short-range order remains, related to the anion vacancies formed at this transition. If the sample is heated in a dynamic vacuum in the electron microscope, one could expect a further elimination of the anions and an increasing amount of anion vacancies in the tunnels. It is accompanied by a progressive monoclinic distortion, similar to that in $Bi_6Rh_{12}O_{29}$, which also contains a significant amount of anion vacancies in the subsystem **II** according to the $[BiO_{0.833}]_3[Rh_6O_{12}]$ formula.[22]

To the best of our knowledge, the $[SrF_{0.8}(OH)_{0.2}]_{2.526}$-$[Mn_6O_{12}]$ crystal structure provides the first example of intergrowth between the rock-salt and todorokite-type structures in manganites, where different repeat periods along the *c*-axis of the $[Mn_6O_{12}]$ framework and the [Sr,(F,OH)] columns raise incommensurability. Thus, the chemical composition of the $[AX]_{4\gamma}[Mn_6O_{12}]$ compounds and the misfit between the subsystems are mutually dependent. One can expect complex behavior of these compounds upon isovalent substitution of the Sr cations by smaller Ca or larger Ba cations: compression or expansion of the rock-salt columnar fragment changes the volume ratio between the [AX] and $[Mn_6O_{12}]$ subsystems, causing simultaneous reduction or oxidation of the Mn cations, which in turn would result in an expansion or compression of the $[Mn_6O_{12}]$ framework. Such solid solutions invite further detailed investigation in order to formulate major structural trends for this class of compounds. It can be also expected that the discovered scheme of intergrowth between the rock-salt fragments and todorokite-type framework will lead to a family of tunnel transition metal oxides with various tunnel size.

Acknowledgment. This work was supported in part by the IAP V-1 program of the Belgium government and the RFBR projects 04-03-32785-a, 05-03-34812-MF-a, and 03-03-32707-a.

Supporting Information Available: Crystallographic data in CIF format for $[SrF_{0.8}O_{0.1}]_{2.526}[Mn_6O_{12}]$ at 400 °C; determination of fluorine content by electromotive force (EMF) measurements (PDF). This material is available free of charge via the Internet at http://pubs.acs.org.

CM062508S